RESEARCH ARTICLE | APRIL 18 2024

Comparison of Mg-based liquid metal ion sources for scalable focused-ion-implantation doping of GaN

Michael Titze ; Aaron Katzenmeyer ; Sam Frisone ; James A. Ohlhausen; Anthony Flores ; DeAnna Campbell ; Bingjun Li ; Yongqiang Wang ; Jung Han ; Edward S. Bielejec ; Rachel S. Goldman

AIP Advances 14, 045326 (2024)
https://doi.org/10.1063/5.0198791

Comparison of Mg-based liquid metal ion sources for scalable focused-ion-implantation doping of GaN

Cite as: AIP Advances 14, 045326 (2024); doi: 10.1063/5.0198791
Submitted: 19 January 2024 • Accepted: 25 March 2024 •
Published Online: 18 April 2024

Michael Titze,[1,a] Aaron Katzenmeyer,[1,2] Sam Frisone,[3] James A. Ohlhausen,[1] Anthony Flores,[1] DeAnna Campbell,[1] Bingjun Li,[4] Yongqiang Wang,[5] Jung Han,[4] Edward S. Bielejec,[1] and Rachel S. Goldman[3]

AFFILIATIONS

[1] Sandia National Laboratories, Albuquerque, New Mexico 87185, USA
[2] National Institute of Standards and Technology, Gaithersburg, Maryland 20899, USA
[3] Department of Materials Science and Engineering, University of Michigan, Ann Arbor, Michigan 48109, USA
[4] Department of Electrical Engineering, Yale University, New Haven, Connecticut 06511, USA
[5] Los Alamos National Laboratory, Los Alamos, New Mexico 87545, USA

Note: This paper is part of the Special Issue on the Novel Applications of Focused Ion Beams–Beyond Milling.
[a] **Author to whom correspondence should be addressed:** mictitz@sandia.gov

ABSTRACT

We compare the suitability of various magnesium-based liquid metal alloy ion sources (LMAISs) for scalable focused-ion-beam (FIB) implantation doping of GaN. We consider GaMg, $MgSO_4 \bullet 7H_2O$, MgZn, AlMg, and AuMgSi alloys. Although issues of oxidation (GaMg), decomposition ($MgSO_4 \bullet 7H_2O$), and excessive vapor pressure (MgZn and AlMg) were encountered, the AuMgSi alloy LMAIS operating in a Wien-filtered FIB column emits all Mg isotopes in singly and doubly charged ionization states. We discuss the operating conditions to achieve <20 nm spot size Mg FIB implantation and present Mg depth profile data from time-of-flight secondary ion mass spectrometry. We also provide insight into implantation damage and recovery based on cathodoluminescence spectroscopy before and after rapid thermal processing. Prospects for incorporating the Mg LMAIS into high-power electronic device fabrication are also discussed.

INTRODUCTION

Due to their potential for high breakdown voltage and low on-resistance, GaN-based electronic devices are promising for high-power and high-frequency electronics.[1] Vertical GaN p-i-n devices are expected to offer improved thermal management and reduced leakage current in comparison to their lateral counterparts;[2] however, typical etching and regrowth processes introduce interfacial impurities that limit control of dopant profiles.[3] Thus, a strategy for both vertical and lateral dopant selectivity, without the need for etching and regrowth, is essential for the development of high-quality vertical GaN devices.

Focused ion beams (FIBs) are routinely used for micro- and nano-electronics modification and fabrication, for example, in circuit repair,[4] in mask repair,[5,6] and, more recently, for creating optically active impurities in quantum materials.[7–12] Different techniques for generation of FIBs are available, each one with its own advantages and drawbacks. While gas field ionization sources excel with minimum spot sizes, the limitation to few gases makes them have only niche applications.[13] Plasma sources offer an advantage in terms of high beam current while being able to maintain relatively small spot sizes, making them interesting for large milling applications.[14,15] Finally, liquid metal based FIBs have long been used for TEM sample fabrication, although standard Ga sources pose difficulties due to contamination of the sample by Ga interdiffusion.[16] Development of additional liquid metal alloy ion sources (LMAISs) promises availability of a variety of ion species, allowing tailoring of the ion to the specific application.[17]

Here, we compare the suitability of GaMg, $MgSO_4 \bullet 7H_2O$, MgZn, AlMg, and AuMgSi alloys for scalable focused-ion-beam (FIB) implantation doping of GaN. While a GaMg source is reported in the literature,[18,19] we have found fabrication of this source difficult due to the rapid oxidation of Ga and Mg when exposed to air. After a brief discussion of the issues of oxidation (GaMg), decomposition ($MgSO_4 \bullet 7H_2O$), and excessive vapor pressure (MgZn and AlMg) that prevented use of these alloys as a Mg LMAIS operating in a Wien-filtered FIB column, we describe the fabrication and characterization of a novel LMAIS based on a AuSi eutectic with Mg added as an impurity, following a procedure previously demonstrated by us.[20] The AuSiMg LMAIS is shown to emit all Mg isotopes, allowing tailoring of the hyperfine levels for quantum applications.[21] In addition, the AuSiMg LMAIS has a spot size of 15 × 17 nm^2 with >10 pA beam current. We also present Time-of-Flight Secondary Ion Mass Spectrometry (ToF-SIMS) and cathodoluminescence (CL) data collected from GaN layers following FIB implantation. To examine the activation of Mg dopants in GaN, we compare the pristine and implanted regions before and after rapid-thermal processing (RTP). Many dopant activation studies of Mg in GaN have been performed.[2–4] These studies indicate that Mg activation saturates at temperatures greater than 1000 °C. To avoid decomposition of GaN at high temperature, we limit our annealing temperature to 1100 °C. The opportunities and challenges associated with using this scalable Mg LMAIS source for Mg doping of GaN are discussed.

MATERIALS AND METHODS

Liquid metal alloy ion source (LMAIS) tip fabrication

In preparation for fabrication of LMAIS tips, the source materials were melted in a ceramic boat within a high vacuum (1×10^{-5} Torr) source preparation unit. To remove contaminants prior to dipping in the alloy melt, the W tip is Joule heated until it is glowing yellow (1400 C). The melt is moved toward the tip three times to ensure uniform wetting of the tip surface and good filling of the reservoir. During dipping, the tip temperature decreases and the material freezes onto the tip since the tip is heated via a constant current supply and the resistance of the tip decreases by addition of the alloy, leading to less heating power at the tip. After dipping of the tip, the ceramic boat is cooled back to room temperature and a Faraday cup (FC) is put in place underneath the tip. A high voltage is applied to the tip, and the heating current is increased until the alloy is liquid, leading to field ionization of the liquid metal. The FC remains grounded and is hooked up to a current meter to measure the emission current from the tip as an initial test of whether LMAIS fabrication is successful. Following measurement of LMAIS emission current, the heating current to the tip is turned off to let the tip cool down, and the tip is removed from the vacuum chamber. The filled LMAIS tip is installed in a Raith VELION focused ion beam (FIB) column. The FIB has a Wien (E × B) filter element, which allows resolving isotopes with $m/\Delta m > 30$.

MOCVD growth of UID-GaN for implantation

In preparation for Mg implantation, 3.6 μm of unintentionally doped (UID) GaN was grown via metalorganic chemical vapor deposition (MOCVD) on a commercial n-type GaN substrate, and an array of Au/Ti markers were deposited for FIB alignment and sample navigation.

Time-of-flight secondary ion mass spectroscopy

A ToF-SIMS 5-100 instrument manufactured by Ion-TOF GmbH (Münster, Germany, www.iontof.com) was utilized to perform the ToF-SIMS acquisitions. A surface image was acquired over a 100 × 100 μm^2 region containing the Mg dot array using 50 kV Bi_3^{++} primary ions (~250 nm spot diameter) in the high spatial resolution image mode. Positive secondary ions were collected in six frames containing 512 × 512 pixels with ten shots per pixel per frame. No charge compensation was required in this analysis. The depth profile was performed by analyzing a 50 × 50 μm^2 area using 25 kV Bi_1^+ primary ions in the high concentration (HC)-BUNCHED mode at the center of the dot array while sputtering with a 50 nA, 1 kV O_2^+ beam rastered over a 250 × 250 μm^2 area that included the same dot array in the interlaced mode.

Secondary electron microscopy (SEM) and CL spectroscopy

A Tescan RISE secondary electron microscopy (SEM) equipped with a Gatan MonoCL4 detector was used to collect room temperature CL spectra using a 5 keV acceleration voltage. Details on the CL experiments are discussed in Ref. 22. The spot size and beam current were adjusted to produce a power density of 0.34 W/cm^2. All CL spectra were collected while the electron beam was scanning over a 40 × 40 μm^2 area using a 500 nm blaze diffraction grating. CL spectra were collected using a 500 nm blaze diffraction grating at a wavelength range of 300–750 nm (1.66–4.13 eV) and step size of 5 nm. To reduce the presence of hydrocarbons, samples were ultrasonically cleaned in trichloroethylene, acetone, and isopropyl alcohol for 6 min in each solvent and then plasma cleaned using H_2/O_2 plasma for 5 min.

LMAIS alloy selection

For these studies, several commercial alloys were acquired from ACI Alloys (GaMg and AuSiMg) and Goodfellow, Inc. (AlMg and MgZn). Magnesium sulfate heptahydrate ($MgSO_4 \bullet 7H_2O$) was received in crystalline form.

Initial experiments were performed with GaMg as success was reported previously with this alloy.[18] Pieces of the alloy with compositions of 99/1 and 90/10 atomic % exhibited a black scale on the surface. Used as-is, the scale persists at the surface of the molten alloy and inhibits wetting of the W tip. The scale can be easily removed by mechanical polishing. Polished GaMg (90/10 atomic %) material was melted and loaded onto the W tip and reservoir upon dipping. Due to the low melting point of Ga and the inability to cool the molten metal, fabrication of a high-Ga content GaMg source took prohibitively long since the material needed to be kept under vacuum or an inert atmosphere while it was liquid due to the rapid oxidation of the liquid surface. Upon cooling, the material was atypically rough for an LMAIS [see Fig. 1(a) inset], consistent with solid inclusions. Nonetheless, an emission current of 13 μA was realized with this source with an extraction voltage of 9.57 kV and a Joule heating power of 0.631 V × 4.254 A. A mass spectrum collected in

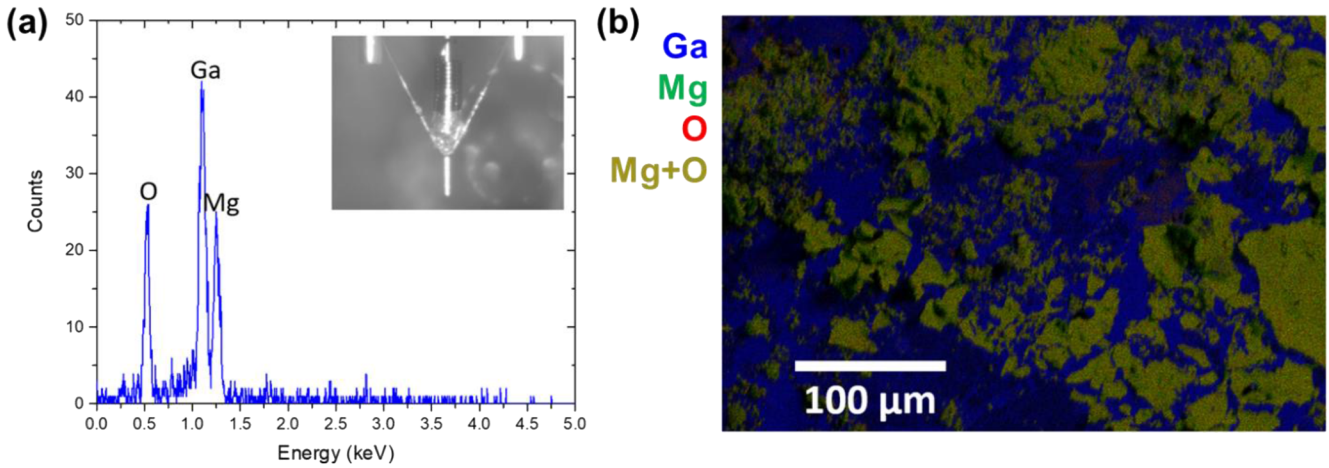

FIG. 1. (a) EDS spectrum showing the characteristic lines of O, Ga, and Mg. Inset: Optical microscopy image collected *in situ* during the GaMg (90/10 atomic %) source preparation. (b) EDS encoded scanning electron microscopy image of the source material. Oxygen is denoted as red, Mg as green, and Ga as blue channel of the image. Mg and Ga are separated (lack of cyan regions), and Mg binds with O, forming large yellow regions.

the Raith VELION indicated that only Ga ions were present in the beam. The material from the source was imaged using a scanning electron microscope and was inhomogeneous. Energy dispersive spectroscopy (EDS) of the material was performed and indicated that O was present in regions containing Mg [Figs. 1(a) and 1(b)]. We conclude that the Mg used in this preparation is primarily in the form of a stable magnesium oxide and does not contribute to a measurable ion current.

Other low melting point alloys of Mg, AlMg and MgZn, were used for LMAIS preparation. Unfortunately, the high vapor pressures of these materials were cumbersome for realizing a useful source. Substantial material evaporation in high vacuum rapidly coated view ports used to facilitate source preparation by dipping the W tip in a boat of molten alloy. Wetting of the W tip with the MgZn alloy was achieved at higher pressure (1 Torr, N_2); however, high vacuum is required for focused ion beam applications to avoid significant energy spread of ions due to collisions with background gas. The MgZn source emitted briefly at high vacuum but failed shortly thereafter as the material was lost by evaporation.

Magnesium sulfate heptahydrate was considered to give the reported emission of ionic liquid ion sources (ILISs) such as 1-ethyl-3-methylimidazolium tetrafluoroborate (EMI-BF_4)[28] and our ability to observe ILIS emission in our apparatus. $MgSO_4 \bullet 7H_2O$, unlike the ILIS, requires heating to reach the molten state; however, this is a trivial task in an LMAIS system. $MgSO_4 \bullet 7H_2O$ was loaded into a standard W emitter's reservoir and heated. Insufficient material reached the W tip prior to dehydration or decomposition, and no emission was observed. The results of different Mg source materials are summarized in Table I.

The I–V curve of the AuSiMg tip is shown in Fig. 2(a), exhibiting linear behavior within a range of extraction energies. The threshold voltage is 6.8 kV, similar to other LMAIS tips. When an extraction voltage of above 8.5 kV is applied, the emission becomes unstable and the tip only emits intermittently. The mass spectrum of the tip after installation into the VELION FIB, operated with 35 kV acceleration potential, is shown in Fig. 2(b). The mass spectrum shows emission of all Mg isotopes in both singly and doubly charged states, allowing for implantation of up to 70 keV Mg using our accelerator. In addition, peaks for Au and Si are visible in the

TABLE I. Summary of literature melting temperatures and observed failure modes for all LMAIS source materials.

Alloy	Melting point	Failure mode
GaMg	(99/1 at. %) 30 °C (90/10 at. %) 170 °C[23]	Only Ga emitted and Mg oxidized observed by EDS
MgZn (70/30 at. %)	350 °C[24]	High vapor pressure
AlMg (62/38 at. %)	455 °C[25]	High vapor pressure
$MgSO_4 \bullet 7H_2O$	250 °C[26,27]	Decomposition
AuSiMg	380 °C	N/A: successfully used as LMAIS

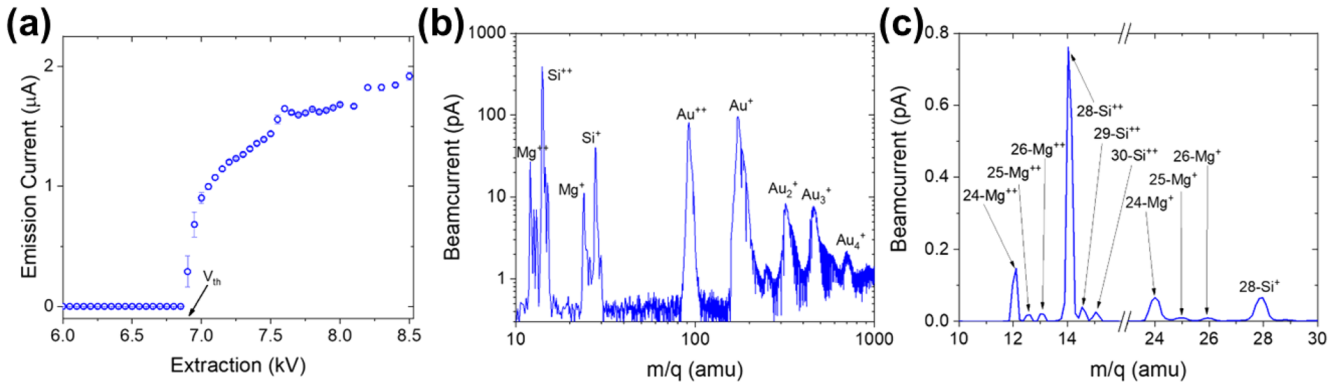

FIG. 2. (a) I–V characteristic of the AuSiMg source showing the threshold voltage at 6.8 kV and linear behavior of the emission current above 7 kV extraction potential. The error bars denote the standard deviation of the current within a 60 s period. (b) Mass spectrum of the AuSiMg LMAIS taken in a VELION column outfitted with a Wien filter element. (c) Gaussian fit of Mg and Si mass spectrum peaks. The relative peak strength, measured by the peak area, matches the natural abundance of Mg isotopes.

mass spectrum. The part of the spectrum containing the Mg peaks is fitted with Gaussians, as shown in Fig. 2(c), and we find that the relative current ratio of the doubly charged Mg isotopes matches the ratio of naturally abundant Mg. We did not run the source until its end of life. However, based on manufacturer specifications on AuSi eutectic tips of this geometry, and our own experience with alkali element containing tips, the lifetime of the tip is expected to be 2000 μAh.[20] Compared with a AuSiLi source, which was found to slowly degrade while being exposed to air, we do not have reason to believe that this tip suffers from the same degradation since even after multiple months of being exposed to air, the source started at conditions comparable to those during initial fabrication of the tip and ran in a stable manner for multiple hours at a time.

RESULTS AND DISCUSSION

The spot size achievable on the VELION using a Mg beam was measured by scanning the beam over a sample implanted with a high contrast checkerboard pattern and detecting secondary electrons (SEs) as the beam is scanned. The resulting SE map is shown in Fig. 3(a) with additional high-resolution linecuts taken at the indicated locations. The linecuts are shown in Fig. 3(b), where the blue (red) datapoints correspond to the linecut along the X (Y) direction. In addition, the 80/20% intensity levels are indicated as black dashed lines. From the 80/20% intensity levels, the full-width at half maximum (FWHM) of the spot size is measured. The spot size in X (Y) is measured to be 15 (17) nm.

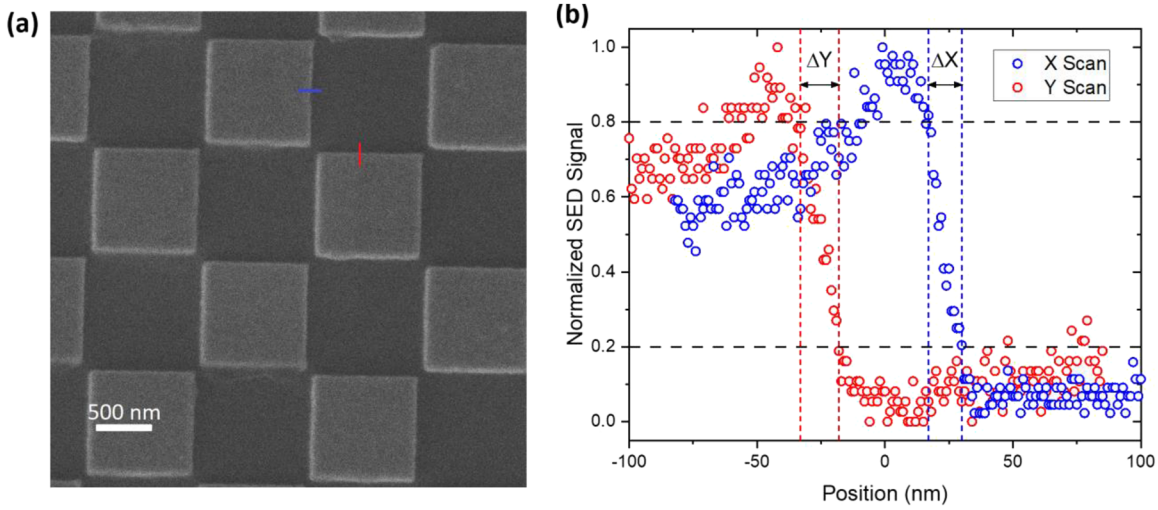

FIG. 3. (a) Picture of a Chessy sample. The red and blue lines show the locations for the spot size measurement. (b) High resolution scans over the areas marked in (a) used to evaluate the beam spot size.

An array of dots was implanted with 70 keV Mg^{++} using the AuSiMg LMAIS at an ion fluence of 10^{17} ions/cm^2. ToF-SIMS was performed to analyze the vertical and lateral distribution of Mg. By averaging over the implanted area, a depth profile was constructed in Fig. 4(a), which was compared with SRIM simulations and indicated an extended implantation depth compared to the expected implant profile. In addition, a defocusing effect was observed, with an enhanced impact for heavier Mg isotopes, as seen in Figs. 4(b)–4(e).

An additional Au/Ti patterned UID-GaN-on-n-GaN sample was implanted with 70 keV Mg^{++} in checkerboard patterns consisting of alternating 70 × 70 and 50 × 50 μm^2 squares, with and without Mg FIB implantation. Different regions in the sample were implanted with a range of ion fluences from 1 × 10^{12} to 1 × 10^{15} ions/cm^2, resulting in a peak Mg concentration of 10^{17}–10^{20} ions/cm^3, calculated via Stopping and Range of Ions in Matter (SRIM) simulations. These doping levels have been previously shown to generate optically active color centers in GaN.[29] The implantation plan is shown in Fig. 5(a), where implant regions are denoted by blue areas. SE images of the as-implanted sample clearly show the implanted checkerboard pattern, as shown in Fig. 5(b). Following removal of the Au/Ti markers and annealing of the sample via RTP at 1100 °C in N_2 for 30 s and 10 min 30 s, we observe a decrease in the SE contrast with each annealing step, as shown in Figs. 5(c) and 5(d), respectively. The dark regions along columns D, E, F in Figs. 5(b)–5(d) denote areas from which CL spectra are collected, leading to a reduction in the SE yield, likely due to local charging of the sample surface.

For all regions, the CL spectra reveal GaN near-band edge (NBE) emissions at 3.4 eV (Fig. 6). The intensity of NBE emission is highest in the pristine regions, especially those in the vicinity of the two lowest ion fluences. Furthermore, in pristine regions adjacent to the two lowest ion fluences, we observe CL emissions at 2.85 and 2.2 eV. As discussed in Ref. 22, we attribute these emissions to impurity-related donor–acceptor pairs and yellow luminescence, respectively. The reduced SE image intensity and limited CL emission in the vicinity of the highest ion fluences suggest incomplete Mg dopant activation. Without annealing, only intrinsic NBE emission is observed in the low-fluence implanted region, as shown in Fig. 6(b), while the adjacent UID-type GaN exhibits clear yellow

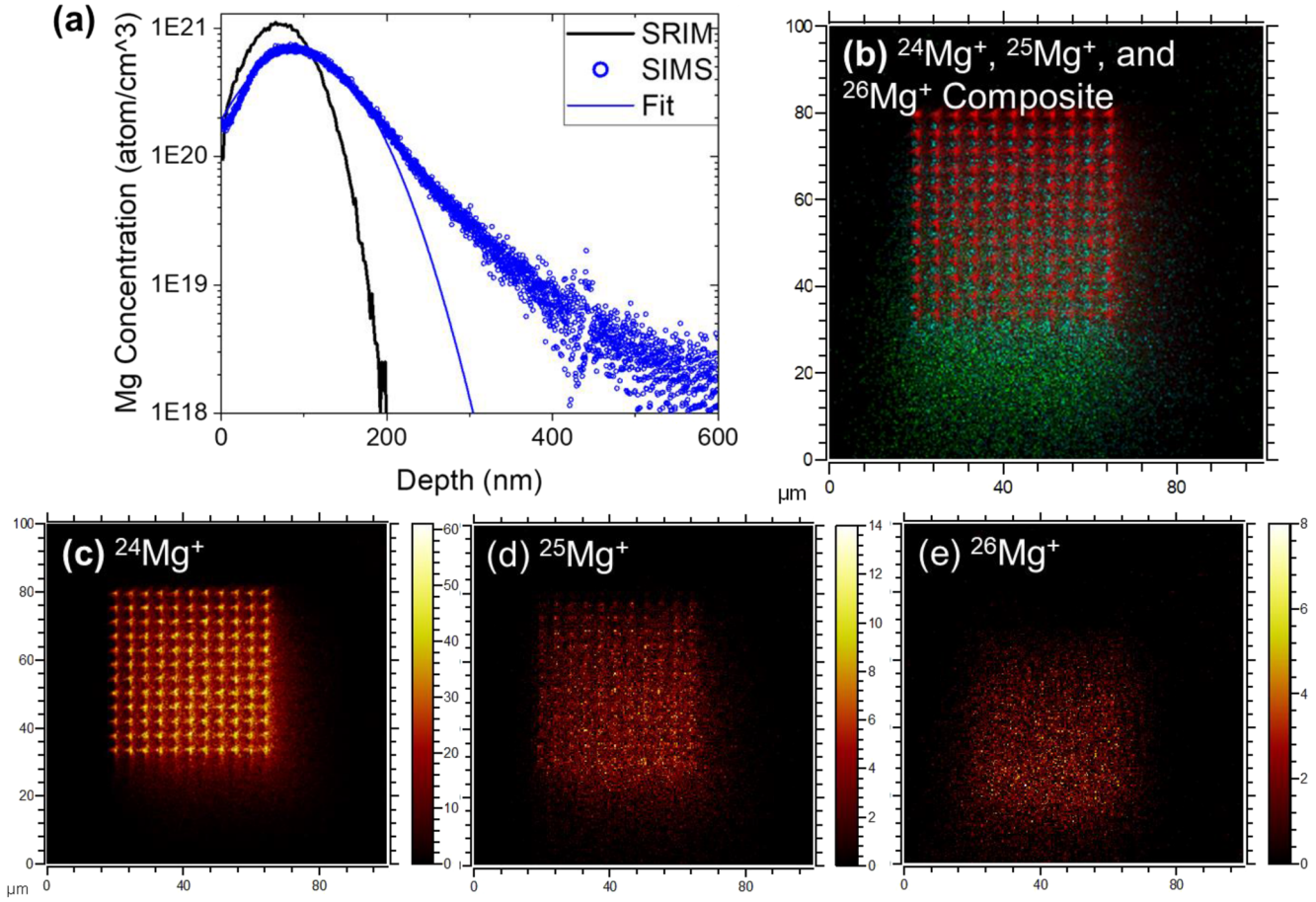

FIG. 4. (a) Range of 70 keV Mg^{++} ions in GaN simulated by SRIM and measured via ToF-SIMS. The solid blue line is a Gaussian fit to the ToF-SIMS data. (b) Composite ToF-SIMS image of $^{24}Mg^+$, $^{25}Mg^+$, and $^{26}Mg^+$ isotopes. ToF-SIMS image of (c) $^{24}Mg^+$, (d) $^{25}Mg^+$, and (e) $^{26}Mg^+$ distribution.

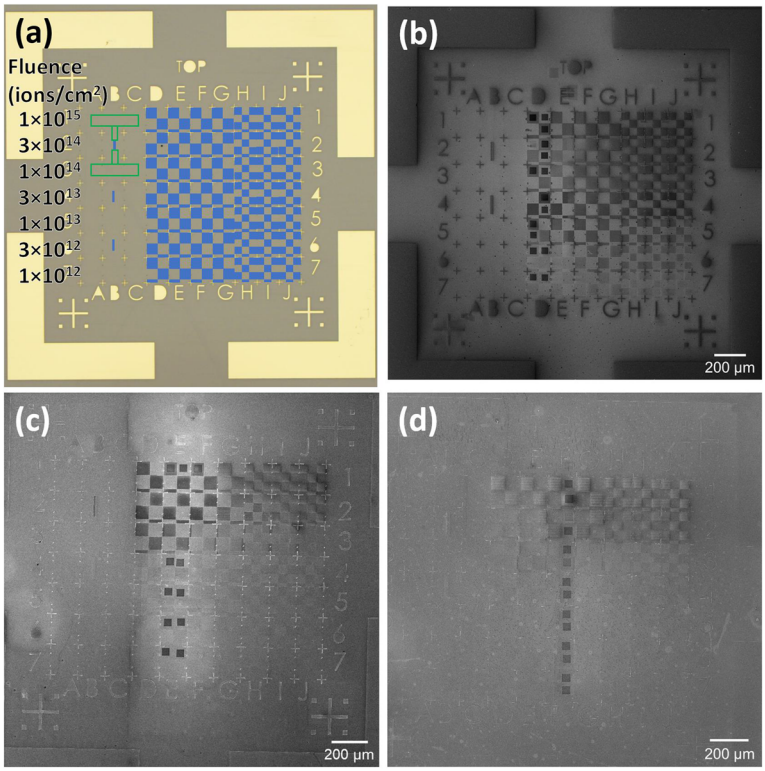

FIG. 5. (a) Microscope image of the GaN wafer after metal patterning and etching. The blue regions denote the implant regions. (b) SE image of the as-implanted sample exhibiting strong SE contrast between implanted and unimplanted regions. The dark regions along column D are areas at which CL spectra are recorded. (c) SE image after annealing in a N_2 atmosphere at 1100 °C for 30 s. (d) SE image after annealing at 1100 °C for an additional 20 30 s cycles, for a total annealing time of 10.5 min.

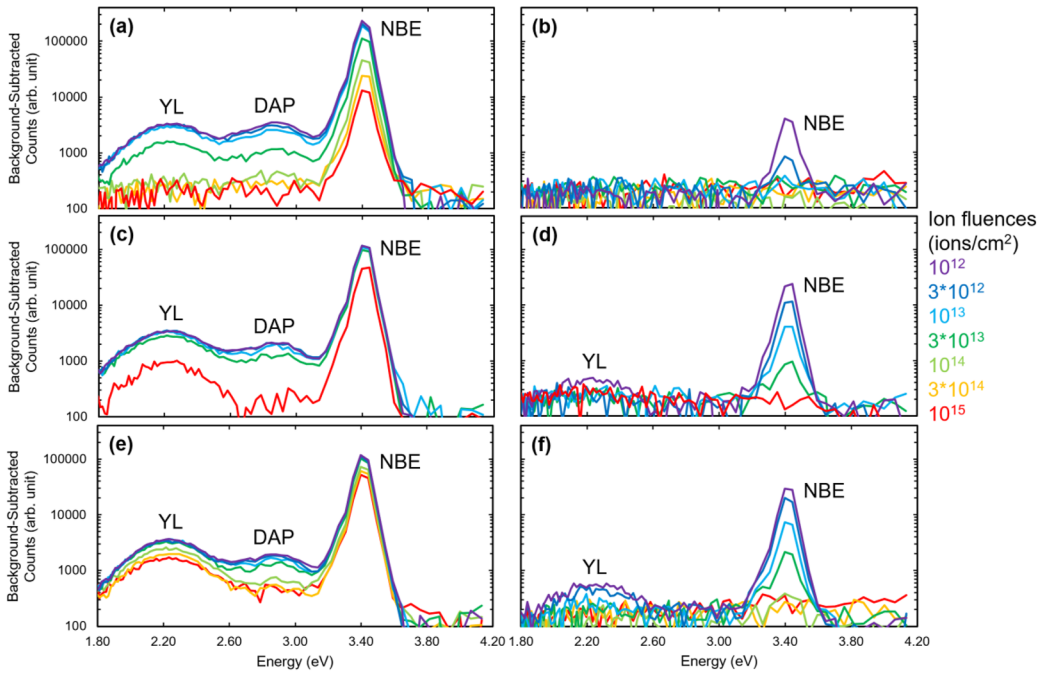

FIG. 6. (a) CL spectra of unimplanted regions of as-implanted sample directly adjacent to implanted areas. (b) CL spectra of as-implanted regions. (c) Unimplanted regions after one round of RTP. (d) Implanted regions after one round of RTP. (e) Unimplanted regions after two rounds of RTP. (f) Implanted regions after two rounds of RTP.

luminescence (YL) and emission due to donor–acceptor pair (DAP) recombination, as shown in Fig. 6(a). Upon annealing the sample, the YL line is partially recovered in the low-fluence implanted regions, up to 3×10^{12} ions/cm^2, as shown in Figs. 6(d)–6(f). In addition, the NBE emission increases with increasing annealing, indicating that the Mg-implanted regions are highly damaged, with successive anneals partially healing the damage. Interestingly, the UID-type regions adjacent to high-fluence implanted regions also show an increase in CL spectrum intensity following annealing, as shown in Figs. 6(c)–6(e). Outdiffusion and redeposition of Mg during the high-temperature annealing step cannot be excluded here;[1] however, they can be excluded as the source of the observed effect of the UID-type region changes since the effect is observed even in the as-implanted sample. From ToF-SIMS measurements, we observed Mg migration up to 1 μm in as-implanted samples; therefore, we expect no impact from Mg implantation damage on adjacent UID-type regions in the as-implanted sample and attribute the suppression of the YL and DAP CL peaks to Mg-based doping of the GaN substrate, leading to charge state suppression of YL and DAP emission.

OPPORTUNITIES AND CHALLENGES

Availability of a stable FIB-based Mg source may enable new prospects for selected-area Mg doping of GaN during GaN growth. While mask-based ion implantation is the *de facto* standard for conventional semiconductor doping, the limited solubility of Mg in GaN limits the doping levels currently achieved.[30–32] High quality GaN is typically grown by molecular beam epitaxy (MBE). For device fabrication, nanoscale localized doping is required, traditionally not possible to achieve during MBE growth. However, by locally irradiating GaN with FIB based Mg, we anticipate increased incorporation efficiency of Mg while maintaining spatial resolution relevant for device fabrication, which will be a part of a follow-on study.

To conclude, we demonstrated how to fabricate a Mg FIB source. Since this source is based on a AuSi eutectic, no issues with oxidation or evaporation are present, in contrast to other Mg FIB sources previously demonstrated. The Mg source performs similar to other AuSi eutectic sources and produces <20 nm spot size. The source is used for Mg implantation into high-quality GaN. We find that as-implanted CL emission is strongly suppressed and ascribe this suppression to implantation damage. Upon annealing of the sample, we observe an increase in the CL emission in the implanted regions. We also observe changes in the CL emission in the nearby UID-regions, which are ascribed to the charge state of relevant defects being suppressed from Mg implantation.

ACKNOWLEDGMENTS

This work was performed, in part, at the Center for Integrated Nanotechnologies, an Office of Science User Facility operated for the U.S. Department of Energy (DOE) Office of Science. Sandia National Laboratories is a multimission laboratory managed and operated by National Technology and Engineering Solutions of Sandia, LLC, a wholly owned subsidiary of Honeywell International, Inc., for the U.S. DOE's National Nuclear Security Administration, under Contract No. DE-NA-0003525. The views expressed in the article do not necessarily represent the views of the U.S. DOE or the United States Government. NSF Support for the Tescan RISE SEM (Grant No. NSF-DMR-1625671) at the University of Michigan is acknowledged. R.S.G. and S.F. also acknowledge the assistance of the staff at the Michigan Center for Materials Characterization. Support of Grant No. NSF-DMR-1625671 for the Tescan RISE SEM is also acknowledged. R.S.G., S.F., B.L., and J.H. were supported in part by the Advanced Research Projects Agency-Energy (ARPA-E), U.S. Department of Energy (Grant No. DEAR0000871), as part of the PNDIODES Program managed by Dr. Isik Kizilyalli. R.S.G. and S.F. were also supported in part by the Air Force Office of Scientific Research through the Multidisciplinary University Research Initiative, Award No. FA9550-23-1-033.

AUTHOR DECLARATIONS

Conflict of Interest

The authors have no conflicts to disclose.

Author Contributions

Michael Titze: Conceptualization (lead); Data curation (lead); Formal analysis (lead); Investigation (lead); Methodology (lead); Supervision (lead); Validation (lead); Visualization (lead); Writing – original draft (lead). **Aaron Katzenmeyer**: Conceptualization (equal); Data curation (equal); Investigation (equal); Methodology (equal); Writing – review & editing (equal). **Sam Frisone**: Data curation (equal); Formal analysis (equal); Visualization (equal); Writing – review & editing (equal). **James A. Ohlhausen**: Data curation (equal); Investigation (supporting); Methodology (supporting); Visualization (equal); Writing – review & editing (equal). **Anthony Flores**: Conceptualization (supporting); Investigation (equal); Methodology (equal); Writing – review & editing (supporting). **Deanna Campbell**: Data curation (supporting); Investigation (equal); Methodology (equal); Writing – review & editing (equal). **Bingjun Li**: Data curation (supporting); Investigation (equal); Methodology (equal); Writing – review & editing (equal). **Yongqiang Wang**: Conceptualization (equal); Data curation (supporting); Investigation (equal); Methodology (supporting); Writing – review & editing (equal). **Jung Han**: Supervision (equal); Writing – review & editing (equal). **Edward S. Bielejec**: Data curation (supporting); Investigation (supporting); Project administration (equal); Resources (equal); Supervision (equal); Writing – review & editing (equal). **Rachel S. Goldman**: Conceptualization (equal); Data curation (supporting); Investigation (supporting); Project administration (lead); Resources (equal); Supervision (lead); Writing – review & editing (equal).

DATA AVAILABILITY

The data that support the findings of this study are available from the corresponding author upon reasonable request.

REFERENCES

[1] J. Y. Tsao, S. Chowdhury, M. A. Hollis, D. Jena, N. M. Johnson, K. A. Jones, R. J. Kaplar, S. Rajan, C. G. Van de Walle, E. Bellotti, C. L. Chua, R. Collazo, M. E. Coltrin, J. A. Cooper, K. R. Evans, S. Graham, T. A. Grotjohn, E. R. Heller, M. Higashiwaki, M. S. Islam, P. W. Juodawlkis, M. A. Khan, A. D. Koehler, J. H. Leach, U. K. Mishra, R. J. Nemanich, R. C. N. Pilawa-Podgurski, J. B. Shealy, Z. Sitar, M. J. Tadjer, A. F. Witulski, M. Wraback, and J. A. Simmons, "Ultrawide-bandgap semiconductors: Research opportunities and challenges," Adv. Electron. Mater. **4**(1), 1600501 (2018).

[2] T. Pu, U. Younis, H.-C. Chiu, K. Xu, H.-C. Kuo, and X. Liu, "Review of recent progress on vertical GaN-based PN diodes," Nanoscale Res. Lett. **16**(1), 101 (2021).

[3] H. Fu, K. Fu, C. Yang, H. Liu, K. A. Hatch, P. Peri, D. Herath Mudiyanselage, B. Li, T.-H. Kim, S. R. Alugubelli, P.-Y. Su, D. C. Messina, X. Deng, C.-Y. Cheng, R. Vatan Meidanshahi, X. Huang, H. Chen, T.-H. Yang, J. Zhou, A. M. Armstrong, A. A. Allerman, E. T. Yu, J. Han, S. M. Goodnick, D. J. Smith, R. J. Nemanich, F. A. Ponce, and Y. Zhao, "Selective area regrowth and doping for vertical gallium nitride power devices: Materials challenges and recent progress," Mater. Today **49**, 296–323 (2021).

[4] K. B. N. Hooghan, "Device edits and modifications," in *Introduction to Focused Ion Beams: Instrumentation, Theory, Techniques and Practice*, edited by L. A. Giannuzzi and F. A. Stevie (Springer, Boston, MA, 2005), pp. 87–106.

[5] M. E. Schmidt, M. Akabori, H. Mizuta, M. E. Schmidt, M. Akabori, and H. Mizuta, *Nitrogen Ion Microscopy* (IntechOpen, 2018).

[6] F. Aramaki, T. Kozakai, O. Matsuda, O. Takaoka, Y. Sugiyama, H. Oba, K. Aita, and A. Yasaka, "Photomask repair technology by using gas field ion source," Proc. SPIE **8441**, 84410D (2012).

[7] P. Kehayias, J. Henshaw, M. Saleh Ziabari, M. Titze, E. Bielejec, M. P. Lilly, and A. M. Mounce, "A fitting algorithm for optimizing ion implantation energies and fluences," Nucl. Instrum. Methods Phys. Res., Sect. B **500–501**, 52–56 (2021).

[8] N. Delegan, S. J. Whiteley, T. Zhou, S. L. Bayliss, M. Titze, E. Bielejec, M. V. Holt, D. D. Awschalom, and F. J. Heremans, "Deterministic nanoscale quantum spin-defect implantation and diffraction strain imaging," Nanotechnology **34**(38), 385001 (2023).

[9] R. Ebadi, M. C. Marshall, D. F. Phillips, J. Cremer, T. Zhou, M. Titze, P. Kehayias, M. Saleh Ziabari, N. Delegan, S. Rajendran, A. O. Sushkov, F. Joseph Heremans, E. S. Bielejec, M. V. Holt, and R. L. Walsworth, "Directional detection of dark matter using solid-state quantum sensing," AVS Quantum Sci. **4**, 044701 (2022).

[10] V. Chandrasekaran, M. Titze, A. R. Flores, D. Campbell, J. Henshaw, A. C. Jones, E. S. Bielejec, and H. Htoon, "High-yield deterministic focused ion beam implantation of quantum defects enabled by in situ photoluminescence feedback," Adv. Sci. **10**(18), 2300190 (2023).

[11] M. Titze, H. Byeon, A. Flores, J. Henshaw, C. T. Harris, A. M. Mounce, and E. S. Bielejec, "In situ ion counting for improved implanted ion error rate and silicon vacancy yield uncertainty," Nano Lett. **22**, 3212 (2022).

[12] D. Pak, A. Nandi, M. Titze, E. S. Bielejec, H. Alaeian, and M. Hosseini, "Long-range cooperative resonances in rare-earth ion arrays inside photonic resonators," Commun. Phys. **5**(1), 89 (2022).

[13] J. Orloff, M. Utlaut, and L. Swanson, "Field ionization sources," in *High Resolution Focused Ion Beams: FIB and its Applications: The Physics of Liquid Metal Ion Sources and Ion Optics and Their Application to Focused Ion Beam Technology*, edited by J. Orloff, M. Utlaut, and L. Swanson (Springer, Boston, MA, 2003), pp. 5–19.

[14] X. Zhong, C. A. Wade, P. J. Withers, X. Zhou, C. Cai, S. J. Haigh, and M. G. Burke, "Comparing Xe^+pFIB and Ga^+FIB for TEM sample preparation of Al alloys: Minimising FIB-induced artefacts," J. Microsc. **282**(2), 101–112 (2021).

[15] T. L. Burnett, R. Kelley, B. Winiarski, L. Contreras, M. Daly, A. Gholinia, M. G. Burke, and P. J. Withers, "Large volume serial section tomography by Xe plasma FIB dual beam microscopy," Ultramicroscopy **161**, 119–129 (2016).

[16] C. Lehrer, L. Frey, S. Petersen, M. Mizutani, M. Takai, and H. Ryssel, "Defects and gallium-contamination during focused ion beam micro machining," in *2000 International Conference on Ion Implantation Technology Proceedings. Ion Implantation Technology-2000 (Cat. No. 00EX432)* (IEEE, 2000), pp. 695–698.

[17] L. Bischoff, P. Mazarov, L. Bruchhaus, and J. Gierak, "Liquid metal alloy ion sources—An alternative for focussed ion beam technology," Appl. Phys. Rev. **3**(2), 021101 (2016).

[18] J. Cheng and A. J. Steckl, "Mg–Ga liquid metal ion source for implantation doping of GaN," J. Vac. Sci. Technol. B **19**(6), 2551–2554 (2001).

[19] Y. Saito and T. Noda, "Bimetallic cluster cations ejected from a liquid metal ion source: Li–Na and Li–Mg," Z. Phys. D: At., Mol. Clusters **19**(1–4), 129–131 (1991).

[20] M. Titze, D. L. Perry, E. A. Auden, J. L. Pacheco, J. B. S. Abraham, and E. S. Bielejec, "Lithium source for focused ion beam implantation and analysis," J. Vac. Sci. Technol. B **39**(1), 012802 (2021).

[21] I. B. W. Harris, C. P. Michaels, K. C. Chen, R. A. Parker, M. Titze, J. A. Martínez, M. Sutula, I. R. Christen, A. M. Stramma, W. Roth, C. M. Purser, M. H. Appel, C. Li, M. E. Trusheim, N. L. Palmer, M. L. Markham, E. S. Bielejec, M. Atatüre, and D. Englund, "Hyperfine spectroscopy of isotopically engineered group-IV color centers in diamond," PRX Quantum **4**, 040301 (2023).

[22] A. S. Chang, B. Li, S. Wang, S. Frisone, R. S. Goldman, J. Han, and L. J. Lauhon, "Unveiling the influence of selective-area-regrowth interfaces on local electronic properties of GaN *p-n* junctions for efficient power devices," Nano Energy **102**, 107689 (2022).

[23] J. Charles, M. Notin, M. Rahmane, and J. Hertz, "NANCYUN: A laboratory tool for calculation of binary systems," J. Phase Equilib. **13**(5), 497–506 (1992).

[24] C. Niu, M. Liu, C. Li, Z. Du, and C. Guo, "Thermodynamic description on the miscibility gap of the Mg-based solid solution in the Mg–Zn, Mg–Nd and Mg–Zn–Nd systems," Calphad **34**(4), 428–433 (2010).

[25] Y. Zhong, M. Yang, and Z.-K. Liu, "Contribution of first-principles energetics to Al–Mg thermodynamic modeling," Calphad **29**(4), 303–311 (2005).

[26] M. N. Scheidema and P. Taskinen, "Decomposition thermodynamics of magnesium sulfate," Ind. Eng. Chem. Res. **50**(16), 9550–9556 (2011).

[27] American Elements, "Magnesium sulfate heptahydrate," see https://www.americanelements.com/magnesium-sulfate-heptahydrate-10034-99-8.

[28] C. Perez-Martinez, S. Guilet, N. Gogneau, P. Jegou, J. Gierak, and P. Lozano, "Development of ion sources from ionic liquids for microfabrication," J. Vac. Sci. Technol. B **28**(3), L25–L27 (2010).

[29] J.-K. So, C. Soci, W. Gao, and N. I. Zheludev, "Focused-ion-beam implantation of luminescence centers in gallium nitride in optical telecom frequency band," in *2021 Conference on Lasers and Electro-Optics Europe and European Quantum Electronics Conference (CLEO/Europe-EQEC)* (IEEE, 2021), p. 1.

[30] C. A. Hernández-Gutiérrez, Y. L. Casallas-Moreno, V.-T. Rangel-Kuoppa, D. Cardona, Y. Hu, Y. Kudriatsev, M. A. Zambrano-Serrano, S. Gallardo-Hernandez, and M. Lopez-Lopez, "Study of the heavily p-type doping of cubic GaN with Mg," Sci. Rep. **10**(1), 16858 (2020).

[31] G. Cheng, "The difficulty and solution of Mg-doped in GaN," IOP Conf. Ser.: Mater. Sci. Eng. **729**(1), 012002 (2020).

[32] P. Kozodoy, H. Xing, S. P. DenBaars, U. K. Mishra, A. Saxler, R. Perrin, S. Elhamri, and W. C. Mitchel, "Heavy doping effects in Mg-doped GaN," J. Appl. Phys. **87**(4), 1832–1835 (2000).